

# Constitutive Equations of Piezoelectric Layered Beams with Interdigitated Electrodes

Nguyen, Cuong Hung; Hanke, Ulrik; Halvorsen, Einar

Nguyen, C. H., Hanke, U. & Halvorsen, E. (2018). Constitutive equations of piezoelectric layered beams with interdigitated electrodes. *IEEE Transactions on ultrasonics, ferroelectrics and frequency control*, 65(9). <https://doi.org/10.1109/TUFFC.2018.2844183>

Publisher's version: DOI: [10.1109/TUFFC.2018.2844183](https://doi.org/10.1109/TUFFC.2018.2844183)

© 2018 IEEE. Personal use of this material is permitted. Permission from IEEE must be obtained for all other uses, in any current or future media, including reprinting/republishing this material for advertising or promotional purposes, creating new collective works, for resale or redistribution to servers or lists, or reuse of any copyrighted component of this work in other works.

# The Constitutive Equations of Piezoelectric Layered Beams with Interdigitated Electrodes

Cuong Hung Nguyen, Ulrik Hanke, Einar Halvorsen

**Abstract**—This paper establishes constitutive equations, or linear two-port models, of piezoelectric layered beams with interdigital electrodes (IDE). The effect of the non-trivial field on the transduction is analyzed. Based on conformal mapping techniques, we derive a new analytic expression for the capacitance, the electric field and the electromechanical coupling factor of an anisotropic dielectric with the IDE configuration on top. The IDE capacitance with an anisotropic permittivity can be treated as the one with an isotropic permittivity. The complexity expression of the non-uniform field is simplified to a quadratic form. A correction is required for the transducer's coupling constant. All modifications are expressed analytically. The analytic models are verified against the finite element method. Finally, the two-port models help to compare to devices with other electrode configurations such as beams with a top and bottom electrode (TBE).

**Index Terms**—constitutive equations, piezoelectric, electromechanical coupling, IDE, conformal mapping, thin-film.

## I. INTRODUCTION

MANY solid state devices utilize piezoelectric sensors, actuators, and transducers in their designs, e.g. energy scavengers [1], accelerometers [2], switches [3], micromirrors [4] and ultrasonic biomedical probes [5]. For some of these applications, a layered beam which consists of many layers of piezoelectric, elastic, insulating or conducting materials is often exploited. In operation, there is an electromechanical coupling process in the piezoelectric layers that depends on the whole beam configuration and the material choice of each layer. An obvious question to raise is then how to design the device to achieve the highest coupling.

The constitutive equations or two-port model are a mathematical representation of an electromechanical transducer. For a linear system it can be denoted by a matrix of coefficients relating stimulus and response of the transducer. The stimulus can for example be efforts such as force  $F$  and voltage  $V$ . The responses are then the generalized displacements charge  $Q$  and deflection  $\delta$ .

A piezoelectric two-port can be specified by three parameters: a beam stiffness  $K_s$ , a free capacitance  $C$ , and an electromechanical coupling factor  $\kappa$ . The squared electromechanical coupling factor is defined as the ratio of the output energy to the maximum input energy during a conversion cycle. Hence,  $\kappa^2$  is a figure of merit saying how effective the piezoelectric transducer is in converting energy. Early

works established the two-port model of unimorph and bimorph piezoelectric benders [6], [7]. Those constitutive equations were later used to evaluate the electromechanical coupling for piezoelectric actuators [8].

With modern thin film technology, piezoelectric devices can be miniaturized while retaining excellent piezoelectric properties [9]. The thin-film technology allows a multitude of potential surface electrode configurations. Since different configurations lead to different field distributions, not necessarily uniform inside the piezoelectric films, they exploit the material differently and their performance cannot easily be compared without also taking geometry into account. Typically, the electrodes are arranged such that either of two different couplings are exploited to drive the transducer: the transversal coupling with top and bottom electrode (TBE) configuration which is governed by the piezoelectric constant  $d_{31}$  and the longitudinal coupling with interdigital electrode (IDE) configuration which is governed by the piezoelectric constant  $d_{33}$ . The strongest transduction may be expected in the IDE transducers because the  $d_{33}$  piezoelectric constant is about twice the  $d_{31}$  constant in common materials [10], [11]. Therefore, the  $d_{33}$  concept has attracted much attention for use in, e.g., energy harvesters [12], switches [13], accelerometers [14] and tunable lenses [15].

The well-established two-port model of unimorph bender [6], [8] can apply directly for the transversal coupling transducer. Currently, researchers concentrate on the longitudinal coupling transducer with the IDE configuration. By using energy methods, analytical formulas for the IDE capacitance, total charge and total electrical energy was derived in [16]. The effect of multiple layers of materials was taken into account by modifying the simple parallel plate model. Similarly, the paper [17] treated the stress and capacitance formulas in the simplest forms. In [18] this weakness was recognized and the two-port model was improved with a capacitance model based on conformal mapping [19]. However, the conformal mapping method, as it is normally applied, is limited to isotropic dielectric materials. Hence, the model cannot be directly applied to piezoelectric materials such as lead zirconate titanate (PZT). In [20] the effect of beam width on the effective material constants was discussed. However, the same simple capacitance formula as in [16] and [17] was used. In addition, all these works neglect the fringing effect around the tip of the IDE finger.

In this paper, we make further efforts in completing the two-port model for the IDE transducer. The dependence of effective material constants on width is discussed. We present models that take into consideration the effects of the multilayer

The authors are with the Department of Microsystems, University of South-Eastern Norway, Campus Vestfold, Raveien 215, 3184 Horten, Norway, (e-mail: Einar.Halvorsen@usn.no).

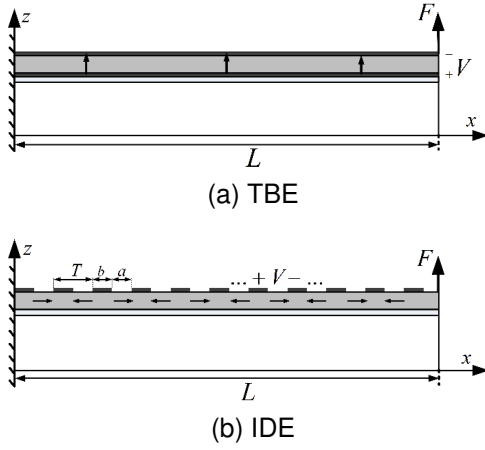


Fig. 1. Piezoelectric cantilever beam with (a)  $d_{31}$  and (b)  $d_{33}$  coupling. The arrows in the grey areas denote polarization direction.

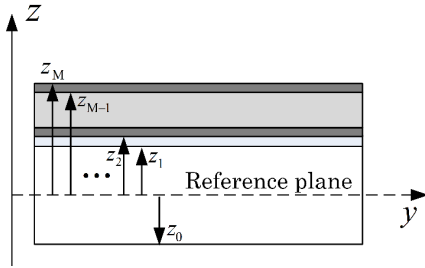


Fig. 2. Cross section of layered beam structure. An example of the TBE device with M layers.

structure. The conformal mapping method is adapted to the anisotropic dielectric by a coordinate transformation [21]. This approach enables a new model based on analytical expressions for the fringing capacitance at the tips of the IDE fingers, the non-uniform electric field and its effect on the transduction. All analytical results are validated against finite element models. Finally, the two-port model enables us to make a comparison between the IDE and TBE transducers.

## II. TWO-PORT MODELLING

### A. The general form of two-port model

In this study, we investigate multilayered cantilever beams like the one shown in Fig.1. A potential difference  $V$  is applied across the electrodes. An external force  $F$  acts at the tip of the beam. Here,  $x$ - $y$ - $z$  coordinate-system axes are device oriented and are different from the crystallographic axes 1-2-3 of the piezoelectric material which are determined by the polarization direction (3 axis) and therefore may vary throughout the device. In general, the layered beams can include arbitrary number of layers of different materials as shown in Fig.2 i.e., an elastic structural material, a piezoelectric layer, some diffusion barriers and/or seed layers, and the IDE or TBE metal electrodes.

Under ideal conditions, the device has no loss or leakage. The energy-conserving transducer is assumed to work in the linear regime. Regardless of whether the configuration is a

TBE Fig.1a or an IDE Fig.1b in static equilibrium, the tip deflection  $\delta$  and electrical charge  $Q$  can be expressed as

$$\begin{pmatrix} \delta \\ Q \end{pmatrix} = \begin{pmatrix} \frac{1}{K_s} & \zeta \\ \zeta & C \end{pmatrix} \begin{pmatrix} F \\ V \end{pmatrix} \quad (1)$$

where  $C$  is the free capacitance and is defined as the capacitance of the structure in the mechanically unloaded state ( $F = 0$ ),  $K_s$  is the beam short-circuit stiffness, and  $\zeta$  is the transducer's coupling constant and is defined as the free tip deflection per unit voltage or the short-circuit charge per unit force [6], [22]. The electromechanical coupling factor  $\kappa$  is

$$\kappa = \zeta \sqrt{\frac{K_s}{C}}, \quad 0 \leq \kappa^2 \leq 1. \quad (2)$$

### B. Governing equations

The governing equations are a starting point in establishing the constitutive equations for the beam. First, some assumptions should be addressed [23] :

1. Each layer is purely linear elastic or piezoelectric.
2. All parts of the structure are in static equilibrium.
3. There is no slip at interfaces between layers.
4. Beam thickness is always much smaller than the beam radius of curvature.

As in [24], we distinguish two special cases: a *narrow beam* i.e., a beam with width much smaller than its length and a *wide beam* i.e., a beam with width much larger than its length. These two cases are treated respectively with plane stress and plane strain constitutive equations. As mentioned in [24], this distinction is motivated by the small Searle parameter [25] and by Swansons conclusion for homogeneous beams [26] that the wide-to-narrow beam transition is independent of the thickness. Intermediate cases of width to length do of course occur, but would have to be treated by plate theory if the limiting cases are not accurate enough.

The effective Young's modulus  $Y$ , the piezoelectric coupling constants  $d$ , and the dielectric constant  $\varepsilon$  for  $d_{31}$  (3,4) [27] and  $d_{33}$  (5,6) coupling are defined as

$$Y = \begin{cases} \frac{1}{s_{11}^E} & \text{narrow beam} \\ \frac{1}{s_{11,\text{eff}}^E} = \frac{s_{22}^E}{s_{11}^E s_{22}^E - (s_{12}^E)^2} & \text{wide beam,} \end{cases} \quad (3)$$

$$d = \begin{cases} d_{31} & \text{narrow beam} \\ d_{31,\text{eff}} = d_{31} - d_{32} \frac{s_{12}^E}{s_{22}^E} & \text{wide beam.} \end{cases} \quad (4)$$

$$Y = \begin{cases} \frac{1}{s_{33}^E} & \text{narrow beam} \\ \frac{1}{s_{33,\text{eff}}^E} = \frac{s_{22}^E}{s_{22}^E s_{33}^E - (s_{32}^E)^2} & \text{wide beam,} \end{cases} \quad (5)$$

$$d = \begin{cases} d_{33} & \text{narrow beam} \\ d_{33,\text{eff}} = d_{33} - d_{32} \frac{s_{32}^E}{s_{22}^E} & \text{wide beam.} \end{cases} \quad (6)$$

$$\varepsilon = \begin{cases} \varepsilon_{33}^T & \text{narrow beam} \\ \varepsilon_{33,\text{eff}}^T = \varepsilon_{33}^T - \frac{d_{32}^2}{s_{22}^E} & \text{wide beam.} \end{cases} \quad (7)$$

where  $s_{ij}^E$  is the compliance at constant electric field,  $d_{ij}$  is the piezoelectric coupling constant and  $\varepsilon_{ij}^T$  is the dielectric constant at constant stress. The Voigt notation [28] is used. In our analysis, we assume that the piezoelectric material has zero shear-tension coupling, i.e.  $s_{ij}^E = 0$  for  $i = 1, 2, 3$  and  $j = 4, 5, 6$ . This assumption applies to many materials such as those with orthorhombic, cubic, isotropic or hexagonal symmetry [29].

From the assumptions, the normal  $x$ -axis strain in the beam is

$$S(x, z) = u'(x) - zw''(x) \quad (8)$$

where  $u(x)$  and  $w(x)$  are the longitudinal displacement and the transversal deflection of a point at position  $x$  along the beam axis.

Let  $z_m$  denote the lowest coordinate of the  $m^{\text{th}}$  layer along the  $z$ -axis as shown in Fig.2.  $Y_m$ ,  $d_m$ , and  $\varepsilon_m$  are the material parameters of this layer. Starting from the  $d$ -form of the piezoelectric constitutive equations and using the effective constants in (3-7), simplified constitutive equations within a layer can be written

$$T_m(x, z) = Y_m(S(x, z) - d_m E_m(x, z)) \quad (9)$$

$$D_m(x, z) = \varepsilon_m(1 - \kappa_m^2)E_m(x, z) + d_m Y_m S(x, z) \quad (10)$$

where  $\kappa_m^2 = Y_m d_m^2 / \varepsilon_m$  is an electromechanical coupling factor for the material.

The general scheme is to use (8-10) to express the electric displacement  $D_m(x, z)$ , the stress resultants bending moment per unit width

$$M(x) = \sum_{m=0}^{M-1} \int_{z_m}^{z_{m+1}} T_m(x, z) z dz, \quad (11)$$

and axial force per unit width

$$P(x) = \sum_{m=0}^{M-1} \int_{z_m}^{z_{m+1}} T_m(x, z) dz \quad (12)$$

in terms of  $V$ ,  $u'$  and  $w''$  for a section of the beam. Together with beam equilibrium equations, these results can be used to obtain expressions for the parameters of the two-port model stated in (1).

### C. Analysis of the TBE transducer

Similar to the analysis of layered beam bender [27], it is possible to choose the coordinate system such that bending moment does not depend on the axial strain and axial force does not depend on the bending strain. One can show that this decoupling is achieved when

$$\sum_m \bar{z}_m Y_m t_m = 0 \quad (13)$$

where  $t_m = z_{m+1} - z_m$  is the thickness of the  $m^{\text{th}}$  layer and  $\bar{z}_m = (z_{m+1} + z_m)/2$ . This choice enforces the origin of the

coordinate system to be located at the neutral axis of the beam and leads to

$$M(x) = -\hat{K} \frac{\partial^2 w}{\partial x^2} + \hat{\Gamma} \frac{V}{t_p} \quad (14)$$

or

$$\frac{\partial^2 w}{\partial x^2} = -\frac{M(x)}{\hat{K}} + \frac{\hat{\Gamma}}{\hat{K}} \frac{V}{t_p} \quad (15)$$

where the  $t_p$  is the thickness of the piezoelectric layer and

$$\hat{K} = \sum_m Y_m \left[ \frac{I_m}{1 - \kappa_m^2} + t_m \bar{z}_m^2 \right], \quad (16)$$

$$\hat{\Gamma} = \sum_m \bar{z}_m Y_m t_m d_m. \quad (17)$$

Here,  $I_m = t_m^3/12$  is the area moment of inertia per unit width of the  $m^{\text{th}}$  layer.

As the force  $F$  acts at the tip of the cantilever beam,

$$M(x) = -F(L - x). \quad (18)$$

The derivation of the tip deflection is as follows. First, we substitute (18) into (15). Then, the new equation is integrated across the beam length. Finally, boundary conditions, no deflection and no slope at the clamped end, are applied to find all integral constants.

From Gauss's law, the electric displacement within the piezoelectric layer at any cross-section is constant. Hence, the electric displacement can be obtained from (10) for any value of  $z$ . However, since the electric field expression has not been derived yet, calculation of the electric displacement from the average value is more convenient. This average value is found by integrating (10) along the  $z$ -axis:

$$\bar{D}_z(x) = \frac{1}{t_p} \int_{z_p}^{z_{p+1}} D_z(x, z) dz. \quad (19)$$

The total electric charge per unit width is

$$Q = \int_0^L \bar{D}_z(x) dx. \quad (20)$$

Neglecting the small contribution to charge from the axial strain, we arrive at a TBE two-port-model with narrow-beam parameters

$$K_s = \frac{3\hat{K}}{L^3}, \quad (21)$$

$$\zeta = \frac{\bar{z}_p d_{31} L^2}{s_{11}^E \hat{K} 2}, \quad (22)$$

$$C = \varepsilon_{33}^T \left[ 1 + (\alpha_{31} - 1) \kappa_{31}^2 \right] \frac{L}{t_p}, \quad (23)$$

and

$$\kappa^2 = \frac{3}{4} \frac{\alpha_{31} \kappa_{31}^2}{1 + (\alpha_{31} - 1) \kappa_{31}^2} \quad (24)$$

where  $\alpha_{31} = t_p \bar{z}_p^2 / (s_{11}^E \hat{K})$ ,  $\kappa_{31}^2 = d_{31}^2 / (s_{11}^E \varepsilon_{33}^T)$ . Note that  $t_p \bar{z}_p^2 / s_{11}^E$  is a contribution of the piezoelectric layer to the flexural rigidity of the beam (16). The quantity  $\alpha_{31}$  therefore quantifies the relative contribution of the piezoelectric layer to the flexural rigidity. We will refer to it as a flexural rigidity ratio.



Fig. 3. Homogeneous field distribution assumption inside active regions.

The formulas (23) and (24) show that all the dependence of  $C$  and  $\kappa^2$  on the other materials of the stack and their relative positions, i.e. the detailed multilayer structure, is through this flexural rigidity ratio.

For the wide beam, the effective values (3), (4) and (7) should be used instead to obtain its parameters by exactly the same route.

For the specific case of a beam with only one structural elastic layer and one piezoelectric layer, the two-port parameters can be found in [6] and [8]. Our general results (21), (23) and (24) agree with these previous results when setting  $M = 2$ .

### III. IDE TRANSDUCER WITH UNIFORM FIELD

We now consider the IDE structure shown in Fig. 1b. We first assume that the electric field has a homogeneous distribution within the active regions between the electrode fingers and is zero in the passive regions beneath each finger as shown in Fig. 3. We choose the origin of the coordinate system so that the desired decoupling between axial strain and bending moment is achieved in the active regions. With this choice, there will be a small such coupling due to the different orientation of the piezoelectric polarization and due to the presence of a very thin metal-electrode film. We neglect this tiny coupling. Following [24], the governing equation of the cantilever is

$$\frac{\partial^2 w}{\partial x^2} = \begin{cases} -\frac{M(x)}{\hat{K}} & \text{Passive region} \\ \frac{\hat{\Gamma}_2}{\hat{K}_2} \frac{V}{a} - \frac{M(x)}{\hat{K}_2} - M_n \left( \frac{1}{\hat{K}_2} - \frac{1}{\tilde{K}_2} \right) & \text{Active region} \end{cases} \quad (25)$$

The passive and active regions are respectively corresponded to  $x \in [nT, nT+b)$  and  $x \in [nT+b, (n+1)T)$  for integer  $n$ . The flexural rigidity in the passive regions  $\hat{K}$  is given in (16). In active regions, the flexural rigidity is

$$\hat{K}_2 = \sum_m Y_m t_m (\bar{z}_m^2 + t_m^2/12). \quad (26)$$

$$M_n = \frac{1}{a} \int_{nT+b}^{(n+1)T} M(x) dx, \quad (27)$$

is the average moment per unit width and

$$\hat{\Gamma}_2 = \sum_m \bar{z}_m Y_m t_m d_m, \quad (28)$$

$$\tilde{K}_2 = \hat{K}_2 + \hat{K}_{2,\xi} - \frac{\hat{\Gamma}_\xi^2}{\hat{K}_p + \hat{K}_{p,\xi}}, \quad (29)$$

where  $\hat{K}_p = \sum_m t_m Y_m$ ,  $\hat{K}_{p,\xi} = \sum_m t_m Y_m \xi_m$ ,  $\xi_m = \frac{\kappa_m^2}{1-\kappa_m^2}$ ,  $\hat{K}_{2,\xi} = \sum_m t_m Y_m \xi_m (\bar{z}_m^2 + t_m^2/12)$ , and  $\hat{\Gamma}_\xi = \sum_m \bar{z}_m Y_m t_m \xi_m$ .

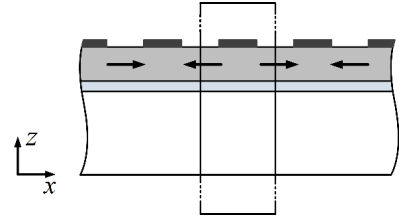


Fig. 4. The total electric charge on an electrode is found by integrating the normal component of the electric displacement vector around the contour.

By inserting (18) into (25), integrating the resulting relation across the beam length, and applying boundary conditions, the tip deflection of the beam is found. From (1), the short-circuit compliance  $1/K_s$  is the ratio of this deflection to the force at zero voltage, i.e.

$$\begin{aligned} \frac{1}{K_s} = & \frac{L(N+1)}{\hat{K}_2} \left[ \frac{a^2}{2} - \frac{a^3 + 3a^2b}{6L} + \frac{NTa}{2} - \frac{N(N+2)T^2a}{6L} \right] \\ & + \frac{L(N+1)}{\hat{K}} \left[ \frac{b^2 + 2ab}{2} - \frac{b^3 + 3ab^2}{6L} + \frac{NTb}{2} - \frac{N(N+2)T^2b}{6L} \right] \\ & - \frac{(N+1)a^3}{12} \left( \frac{1}{\hat{K}_2} - \frac{1}{\tilde{K}_2} \right) \end{aligned} \quad (30)$$

where  $N$  is the number of active regions and  $L = (N+1)T$ .

The coupling constant is the ratio of the deflection to the voltage for zero force, and can be written

$$\zeta = \frac{\bar{z}_p t_p d_{33}}{s_{33}^E \hat{K}_2} \frac{N^2 a}{2} \left( 1 + \left( 1 + \frac{1}{N} \right) \frac{b}{a} + \frac{2}{N} \right) \quad (31)$$

as shown in [24].

Similar to reference [30], the total electric charge per unit width on an electrode of the IDE cantilever can be found from Gauss' law by integrating the normal component of the electric displacement vector around a contour as shown in Fig. 4 and summing over all fingers of the electrode. Neglecting the electric flux outside the piezoelectric material, the contour integral reduces to two integrals across the piezoelectric layers on each side of the finger. Choosing the contour to cross in the middle of the active regions, i.e. at  $x = \bar{x}_n = (n+1/2)T + b/2$ , ensures that the electric displacement field is  $x$ -directed and aligned with or against the normal on those parts of the contour. Hence with  $N$  active regions, the charge is

$$Q = \sum_{n=0}^{N-1} \int_{z_p}^{z_{p+1}} D_x(\bar{x}_n, z) dz. \quad (32)$$

In evaluating this charge, we assume that the electric field is a constant, i.e.  $E(x, z) = E_x = V/a$ . From the charge expression, we can then extract the free capacitance  $C$  as the coefficient of voltage dependence when the force is equal to zero. It is

$$C = \varepsilon_{33,\text{eff}} \frac{N t_p}{a} \quad (33)$$

where we defined an effective permittivity

$$\varepsilon_{33,\text{eff}} = \varepsilon_{33}^T [1 + (\alpha_{33} - 1) \kappa_{33}^2]. \quad (34)$$

and  $\alpha_{33} = \frac{t_p \bar{z}_p^2}{s_{33}^E \hat{K}_2}$ ,  $\kappa_{33}^2 = \frac{d_{33}^2}{s_{33}^E \varepsilon_{33}^T}$ .

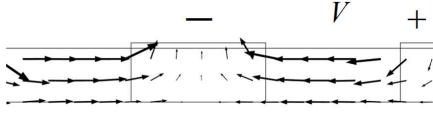


Fig. 5. Inhomogeneous field distribution inside piezoelectric layer.

Since we know  $C$ ,  $K_s$ , and  $\zeta$  the coupling is conveniently quantified in terms of the two-port electromechanical coupling factor (2) which becomes

$$\kappa^2 = \frac{3}{4} \frac{\alpha_{33} \kappa_{33}^2}{1 + (\alpha_{33} - 1) \kappa_{33}^2} \frac{N^3 a^3}{L^3} \left[ 1 + \left( 1 + \frac{1}{N} \right) \frac{b}{a} + \frac{2}{N} \right]^2 \quad (35)$$

where we made the simplification

$$\hat{K} \approx \hat{K}_2 \approx \tilde{K}_2 \quad (36)$$

When  $N$  is large enough, we can further simplify to

$$K_s = \frac{3\hat{K}_2}{L^3} \quad (37)$$

and

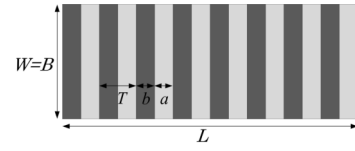
$$\kappa^2 = \frac{3}{4} \frac{\alpha_{33} \kappa_{33}^2}{1 + (\alpha_{33} - 1) \kappa_{33}^2} \frac{a}{T}. \quad (38)$$

Similarly to the TBE device, equations (33), (38) show that  $C$  and  $\kappa^2$  in the IDE device also depend on the detailed layer structure through a flexural rigidity ratio, here called  $\alpha_{33}$ . Equation (38) state that the electromechanical coupling factor of the IDE device also depend on the gap to pitch ratio.

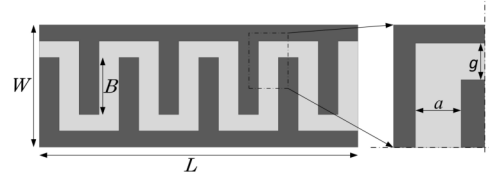
Note that all analysis apply for the narrow structure. For the wide beam, the effective values (5, 6, 7) should be used.

#### IV. IDE TRANSDUCER WITH NON-UNIFORM FIELD

In Section III, the analysis of the second derivative (25) and the capacitance (33) assumes that the electric field has uniform distribution. However, in reality, the field is distributed inhomogeneously [31] as shown in Fig.5. Hence, the parallel-plate capacitance model is poorly justified. The conformal mapping technique (CMT) [32] can be a solution to this problem. The origin of the CMT is that the real and imaginary parts of an analytic function both fulfill the Laplace equation in the complex plane. With an analytic mapping, an analytic function will be mapped to another analytic function on another complex plane. The Laplace equation is then solved in the new plane with simpler standard geometries and boundary conditions. Currently, most available techniques [19], [33] solve the problem for isotropic dielectric materials. However, piezoelectric materials are not isotropic. Hence, Section IV-A will focus on adaption of available CMTs to anisotropic piezoelectric materials in a parallel-strip structure. Section IV-B discusses the non-uniform field and how it affects the transducer coupling constant. Section IV-C presents a new analytic approach to handle the further complexity that arises for the IDE structure when both end-effects and the anisotropy of piezoelectric material are taken into account.



(a) Symmetric configuration



(b) Asymmetric configuration

Fig. 6. Two configuration of the IDE (a) without interconnection lines and (b) with interconnection lines. The dark areas are metal electrodes.

#### A. Capacitance model in an anisotropic piezoelectric material

In the IDE device, the electromechanical coupling mostly originates from the active regions because these regions occupy the largest portion of the piezoelectric structure and have the largest electric field. For the same reason, the capacitance of these regions dominates the total capacitance of the device. Hence, for simplicity, we assume that the passive regions have the same polarisation as the nearest active region. In this section, the top surface of the IDE device Fig.1b has the symmetric configuration without busbars that is shown in Fig.6a. If the beam width  $W$  is not much larger than the gap, the fringing capacitance around the tips of the electrode fingers can be important. The asymmetric configuration Fig.6b should be taken into account. This configuration is analyzed in Section.IV-C

Starting from Gauss law  $\nabla \cdot \vec{D} = 0$ , the piezoelectric constitutive equations and thin beam simplification, the Gauss law equation in the active regions of the piezoelectric layer with narrow-beam parameters is

$$\varepsilon_{33}^T \frac{\partial E_x}{\partial x} + \varepsilon_{11}^T \frac{\partial E_z}{\partial z} + d_{33} \frac{\partial T_p(x, z)}{\partial x} = 0. \quad (39)$$

For the wide beam case,  $\varepsilon_{33}^T$  and  $d_{33}$  should be replaced by  $\varepsilon_{33, \text{eff}}^T$  and  $d_{33, \text{eff}}$  in (6) and (7).

If  $d_{33}$  equals zero or the stress is constant along the  $x$  direction, the last term in (39) is zero. This simpler problem can be found in the literature [21], [34]. Without this simplification, (39) is rewritten using (9) to yield

$$\varepsilon_{33}^T (1 - \kappa_{33}^2) \frac{\partial E_x}{\partial x} + \varepsilon_{11}^T \frac{\partial E_z}{\partial z} + \frac{d_{33}^E}{s_{33}^E} \frac{\partial S(x, z)}{\partial x} = 0. \quad (40)$$

Neglecting the contribution of the axial strain, the strain term in (40) can be replaced by the second derivative using (8), i.e.

$$S(x, z) \approx -z \frac{\partial^2 w}{\partial x^2}. \quad (41)$$

Inserting this simplified strain expression into (9), we get

$$T_m(x, z) = -Y_m \left( z \frac{\partial^2 w}{\partial x^2} + d_m E_m(x, z) \right). \quad (42)$$

For mechanically free boundary conditions, the resultant bending moment (11) is zero. Hence, inserting (42) as the stress terms in (11), we obtain an equation for the second derivative whose solution is

$$\frac{\partial^2 w}{\partial x^2} = -\frac{1}{\hat{K}_2} \int_{z_p}^{z_{p+1}} \frac{d_{33}}{s_{33}^E} z E_x dz. \quad (43)$$

From (43) and (41), (40) is

$$\varepsilon_{33}^T (1 - \kappa_{33}^2) \frac{\partial E_x}{\partial x} + \varepsilon_{11}^T \frac{\partial E_z}{\partial z} + \frac{z d_{33}^2}{\hat{K}_2 (s_{33}^E)^2} \frac{\partial}{\partial x} \int_{z_p}^{z_{p+1}} z E_x dz = 0. \quad (44)$$

We now treat the electric field  $E_x$  as  $z$ -independent in the integral. This approximation is valid when the thickness of the piezoelectric film is much smaller than the active gap. Equation (44) then becomes

$$\varepsilon_{33}^T \left[ 1 + \left( z \frac{\bar{z}_p t_p}{\hat{K}_2 s_{33}^E} - 1 \right) \kappa_{33}^2 \right] \frac{\partial E_x}{\partial x} + \varepsilon_{11}^T \frac{\partial E_z}{\partial z} = 0. \quad (45)$$

This equation has the appearance of a two-dimensional Gauss law with spatially varying permittivity. However, since the thickness of the piezoelectric layer is much smaller than the supporting layer, this variation is negligible. We therefore make the further approximation  $z = \bar{z}_p$  in the bracket and (45) becomes

$$\varepsilon_{33,\text{eff}} \frac{\partial E_x}{\partial x} + \varepsilon_{11}^T \frac{\partial E_z}{\partial z} = 0. \quad (46)$$

Note that the effective permittivity  $\varepsilon_{33,\text{eff}}$  here is the same quantity (34) that we encountered when analyzing the free capacitance (33) using a simpler field assumption. With (46), the capacitance can now be calculated more accurately.

From the field-potential relation  $E_i = -\partial\varphi/\partial x_i$ , (46) becomes

$$\frac{\partial^2 \varphi}{\partial x^2} + \frac{\varepsilon_{11}^T}{\varepsilon_{33,\text{eff}}} \frac{\partial^2 \varphi}{\partial z^2} = 0. \quad (47)$$

We make a change of coordinates from  $(x, z)$  to  $(x, \hat{z})$  such that  $\hat{z} = \hat{z}_m + \sqrt{\varepsilon_{33,\text{eff}}/\varepsilon_{11}^T} (z - z_m)$  within layer no.  $m$  and  $\hat{z}_m$  are constants that make the transformation continuous. With  $\varphi(x, z) = \hat{\varphi}(x, \hat{z})$ , (47) becomes

$$\frac{\partial^2 \hat{\varphi}}{\partial x^2} + \frac{\partial^2 \hat{\varphi}}{\partial \hat{z}^2} = 0 \quad (48)$$

within each layer.

The continuity condition on the normal electric displacement at the interfaces between the piezoelectric and other layers should be valid before and after transformation. Hence,

$$\varepsilon_{11}^T \frac{\partial \varphi}{\partial z} = \sqrt{\varepsilon_{33,\text{eff}} \varepsilon_{11}^T} \frac{\partial \hat{\varphi}}{\partial \hat{z}} \quad (49)$$

must be continuous at  $z_p$  ( $\hat{z}_p$ ) and  $z_{p+1}$  ( $\hat{z}_{p+1}$ ). The quantity  $\varepsilon_{\text{eq}} = \sqrt{\varepsilon_{33,\text{eff}} \varepsilon_{11}^T}$  is treated as an equivalent relative permittivity inside the piezoelectric layer. This means that the anisotropic dielectric material in the  $(x, z)$  coordinate systems can be treated as an isotropic dielectric in the  $(x, \hat{z})$  coordinate system. The equivalent parameters are the relative permittivity  $\varepsilon_{\text{eq}}$ , and the dielectric thickness  $\hat{t}_p = t_p \sqrt{\varepsilon_{33,\text{eff}}/\varepsilon_{11}^T}$ . Once this transformation is made, the capacitance can be calculated by a CMT approach, e.g., Igreja's [19] or Gevorgian's models [33], [35], and [36].

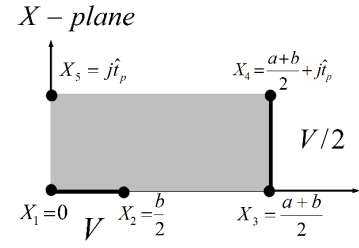


Fig. 7. A representative segment of IDE.

### B. Electric field and coupling constant for the symmetric IDE configuration

By using the same conformal mapping transformations as in [19] for our problem (48), we can derive the electric field in a representative segment of the IDE structure, Fig.7. Representing the two-dimensional electric field by a complex number, it becomes

$$\mathbf{E} = j \frac{V}{a+b} \frac{K(k)}{K(k_1')} \frac{\sqrt{1-k^2 q(X_2)^2}}{\sqrt{q(X_2)^2 - q(X)^2}} \quad (50)$$

where

$$q(X) = \text{sn} \left( \frac{2K(k)X}{a+b}, k \right) \quad (51)$$

with  $X$  is a complex variable in the  $X$ -plane of Fig.7 and  $\text{sn}$  is the Jacobi elliptic function. The elliptic moduli  $k_1$  and  $k_1'$  are given by

$$k_1 = \sqrt{1 - k_1'^2} = \frac{q(X_2) \sqrt{1 - k^2}}{\sqrt{1 - k^2 q(X_2)^2}} \quad (52)$$

and the other elliptic moduli  $k = \sqrt{1 - k'^2}$  can be found from the relation

$$\frac{K(k')}{K(k)} = \frac{2\hat{t}_p}{a+b}. \quad (53)$$

In (50), the signs of the square roots are chosen so that the electric field lines follow the decreasing direction of the electric potential. As the electric field inside the representative segment is known, the electric field at other position of the piezoelectric layer can be found by symmetry.

For the coupling constant  $\zeta$ , (43) shows that only the  $x$ -component of the electric field is of concern. In Section, IV-A, the effective permittivity was approximated by the value at  $z = \bar{z}_p$ . Hence, the electric field at  $z = \bar{z}_p$  is of interest. In the representative segment, this field is expressed as

$$E_x = \text{Re}\{\mathbf{E} [\text{real}(X) + j\hat{t}_p/2]\}. \quad (54)$$

Following the same approach as in [24], a phenomenological quadratic model (PQ model) can be fitted to  $E_x$ , i.e.

$$E_x = \gamma \left[ 1 - \frac{4\beta}{a^2} \left( x - (nT + b) - \frac{a}{2} \right)^2 \right] \times \frac{V}{a} \quad \text{for } nT + b \leq x < (n+1)T$$

$$E_x = 0 \quad \text{elsewhere} \quad (55)$$

where  $n$  is a positive integer. The dimensionless quantity  $\beta$  parametrizes the flatness while  $\gamma$  parametrizes the mid-gap electric field value. These quantities can be found by fitting

(55) at  $x = nT + b + a/2$  and  $x = nT + b$  with the CMT model (54) at  $X = (a + b)/2 + j\hat{t}_p/2$  and  $X = b/2 + j\hat{t}_p/2$ . The result is

$$\gamma = \text{Re} \left[ \mathbf{E} \left( \frac{a+b}{2} + j\frac{\hat{t}_p}{2} \right) \right] \times \frac{a}{V}, \quad (56)$$

$$\beta = 1 - \text{Re} \left[ \mathbf{E} \left( \frac{b}{2} + j\frac{\hat{t}_p}{2} \right) \right] / \text{Re} \left[ \mathbf{E} \left( \frac{a+b}{2} + j\frac{\hat{t}_p}{2} \right) \right]. \quad (57)$$

Since the PQ model (55) is  $z$ -independent, taking this term out of the  $z$ -integration (43), integrating twice along the  $x$ -direction and dividing the result by the applied voltage  $V$ , the transducer's coupling constant  $\zeta$  is expressed as

$$\zeta = \gamma \left( 1 - \frac{\beta}{3} \right) \frac{\bar{z}_p t_p d_{33}}{s_{33}^E \hat{K}_2} \frac{N^2 a}{2} \left( 1 + \left( 1 + \frac{1}{N} \right) \frac{b}{a} + \frac{2}{N} \right). \quad (58)$$

Finally, the electromechanical coupling factor can be calculated since the short-circuit stiffness (37), the free capacitance (Section IV-A) and  $\zeta$  (58) are known.

### C. Capacitance model for the the asymmetric IDE configuration

In IDE devices that are asymmetric due to interconnection lines as shown in Fig.6b, the electrostatic field is complicated around the tip regions of the electrode fingers. The parasitic capacitances contributed from these regions are very different from the values calculated by the parallel plate model. An accurate capacitance calculation should include both field distributions on the IDE surface and inside into the dielectric. This three-dimensional (3D) problem is out of reach of the CMT because the mapping theory only applies to two-dimensional (2D) problems. Therefore, for simplicity, a uniform electrostatic field distribution across the dielectric thickness is assumed. The assumption is suitable for a structure with dielectric thickness much smaller than the IDE pitch. Then the 3D problem is simplified to a 2D problem which can be solved by the CMT.

From Fig.6b, if we know the capacitance  $C_n$  of the small part shown in the inset, the positive integer  $n$  indicates the  $n^{\text{th}}$  active region, the total capacitance  $C$  of the IDE device with  $N$  active regions is

$$C = 2NC_n t_p. \quad (59)$$

To transform the complicated polygonal shape around a corner to a simple rectangle, we apply the conformal transformation in Fig.8 transforming the small part to a parallel plate capacitor. Then,  $C_n$  can be calculated by applying the parallel-plate formula to the rectangle.

The transformation flow in Fig.8 requires two transform steps. First, the polygon in  $z$ -plane is mapped to the upper half-plane in  $\theta$ -plane via the Schwartz-Christoffel (SC) [32] derivative

$$\frac{dz}{d\theta} = c_0 \frac{\sqrt{\theta-1}}{\theta\sqrt{\theta+p}} \quad (60)$$

where the origin  $z = 0$  is chosen at the corner of the IDE finger and is mapped to  $\theta = 1$ . The constants  $c_0 = g/\pi$  and

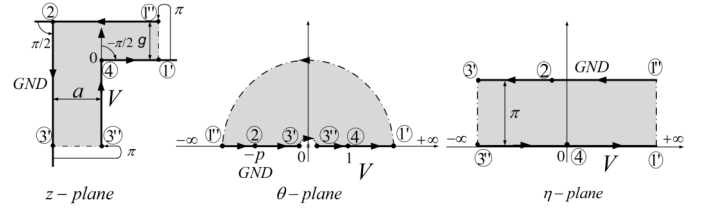


Fig. 8. Conformal mapping flow to transform a polygon into parallel strip lines.

$p = g^2/a^2$  are found by mapping relations given in equations (27.17) and (27.22) of [32]. The integral of (60) is

$$z = c_0 \left[ 2 \sinh^{-1} \sqrt{\frac{\theta-1}{p+1}} - \frac{2 \tan^{-1} \sqrt{\frac{p(\theta-1)}{\theta+p}}}{\sqrt{p}} \right]. \quad (61)$$

In the second step, the upper-half  $\theta$ -plane is mapped to a strip between two parallel lines in the  $\eta$ -plane via a mapping function  $\eta = \ln(\theta)$ . Hence, the capacitance is

$$C_n = \frac{\varepsilon_r \varepsilon_0 (\eta_{1'} - \eta_{3''})}{\pi} = \frac{\varepsilon_r \varepsilon_0}{\pi} \ln \frac{\theta_{1'}}{\theta_{3''}} \quad (62)$$

where  $\theta_{1'}$ ,  $\theta_{3''}$  respectively are images of  $z_{1'}$ ,  $z_{3''}$  in the  $\theta$ -plane. These values can be found in (61).  $\varepsilon_r$  is the relative permittivity of the dielectric layer while  $\varepsilon_0$  is the vacuum permittivity.

Equation (62) only applies directly to an isotropic material. For an anisotropic material that is homogeneous and has the principal directions of the permittivity orthogonal or parallel to the polygonal faces, we can first use the transformation in Section IV-A, introducing an effective permittivity and effective dimensions, to make the problem isotropic.

For the IDE, the polarization direction (3-axis) changes around the corner of a finger as indicated in Fig.9a. The orientation of the permittivity tensor follows the direction of polarization. In order to apply the transformation we therefore split the problem of calculating the capacitance  $C_n$  into two simpler capacitance problems as indicated in the figure. That is, we approximate  $C_n \approx C_{n1} + C_{n2}$  where  $C_{n1}$  and  $C_{n2}$  are the contributions to  $C_n$  related to charges on the thick black lines in Fig.9b and Fig.9c respectively.

When calculating each of the partial capacitances  $C_{n1}$  and  $C_{n2}$ , we treat the spontaneous polarization as uniform as shown in the figure. The largest deviations in assumed permittivity from the stated problem are then found in the regions of the corner with the smallest electric flux density. By this, we expect to have included the dominant contributions to the capacitance and some of the fringing-field effects.

To summarize: each of the partial capacitances is calculated by a transformation to an isotropic problem as in Section IV-A followed by the mapping flow in Fig.8. The capacitances  $C_{n1}$  and  $C_{n2}$  correspond to the two parallel capacitances on the left and the right half-plane of the  $\eta$ -plane separated by the imaginary axis. These capacitances can be calculated using (62)

$$C_{n1} = \frac{\varepsilon_{n1}}{\pi} \ln \frac{1}{\theta_{n1,3''}}; \quad C_{n2} = \frac{\varepsilon_{n2}}{\pi} \ln \theta_{n2,1'} \quad (63)$$

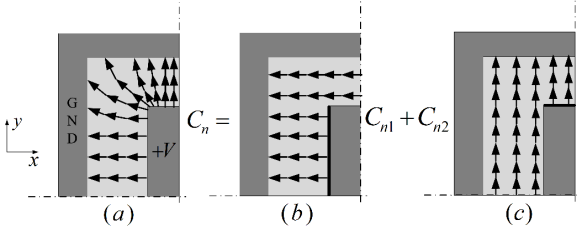


Fig. 9. Capacitance  $C_n$  is split into two different partial capacitances  $C_{n1}$  and  $C_{n2}$ . Each of these has uniform polarization direction as it is shown.

TABLE I

PB(ZR<sub>0.53</sub>Ti<sub>0.47</sub>)O<sub>3</sub> PARAMETERS CALCULATED FROM [10], [37], [38]

Parameters and unit	Notation	Value
Compliance ((TPa) <sup>-1</sup> )	$s_{11}^E = s_{22}^E$	13.8
	$s_{12}^E$	-4.07
	$s_{32}^E = s_{31}^E$	-5.8
	$s_{33}^E$	17.1
Piezoelectric coupling (pm/V)	$d_{31} = d_{32}$	-116.7
	$d_{33}$	224.2
Permittivity	$\epsilon_{11}^T$	1290 $\epsilon_0$
	$\epsilon_{33}^T$	1180 $\epsilon_0$
Material electromechanical coupling factor	$\kappa_{31}^2$	0.09
	$\kappa_{33}^2$	0.28

TABLE II

PB(ZR<sub>0.53</sub>Ti<sub>0.47</sub>)O<sub>3</sub> EFFECTIVE PARAMETERS IN WIDE BEAM CASE

Parameters and unit	Notation	Value
Compliance ((TPa) <sup>-1</sup> )	$s_{11,\text{eff}}^E$	12.6
	$s_{33,\text{eff}}^E$	14.7
Piezoelectric coupling (pm/V)	$d_{31,\text{eff}}$	-151.1
	$d_{33,\text{eff}}$	175.2
Permittivity	$\epsilon_{33,\text{eff}}^T$	1067 $\epsilon_0$
Material electromechanical coupling factor	$\kappa_{31,\text{eff}}^2$	0.19
	$\kappa_{33,\text{eff}}^2$	0.22

where  $\theta_{n1,3''}$  is the image of  $z_{3''}$  in the  $\theta$ -plane of  $C_{n1}$ ,  $\theta_{n2,1'}$  is the image of  $z_{1'}$  in the  $\theta$ -plane of  $C_{n2}$ . The permittivity  $\epsilon_{n1}, \epsilon_{n2}$  correspond to the different polarization orientations for  $C_{n1}$  and  $C_{n2}$  respectively.

Finally, necessary formulas to calculate the two-port parameters for different configurations are summarized in Table III of the Appendix.

## V. NUMERICAL STUDY

### A. Device description

IDE and TBE cantilever beams as shown in Fig.1 are investigated. The analytical and finite element models are compared. We choose a length  $L = 1\text{mm}$  for all the numerical calculations. The cross section of the beam includes a structural elastic layer, a piezoelectric sheet and electrode layers. For the structural layer, we choose  $t_b = 20\mu\text{m}$  thick glass with Young's modulus and Poisson's ratio 74GPa and 0.3 respectively. Glass can be interesting for optical applications. The electrode is 200nm thick platinum with Young's modulus and Poisson's ratio 169GPa and 0.38 respectively. The piezoelectric is PZT 47/53 [37]. The effective transverse and the longitudinal piezoelectric coefficients are respectively  $e_{31,f} = 12\text{C/m}^2$  and  $d_{33,f} = 85\text{pm/V}$ . Other details of the piezoelectric

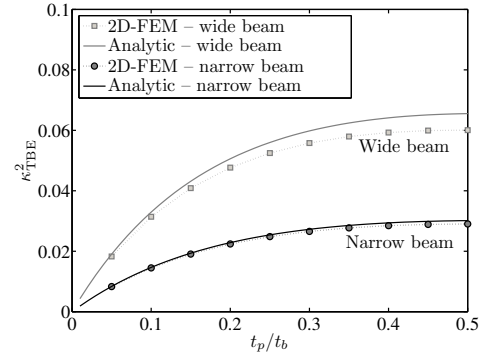


Fig. 10. Electromechanical coupling factor of the TBE device with respect to the film thickness.

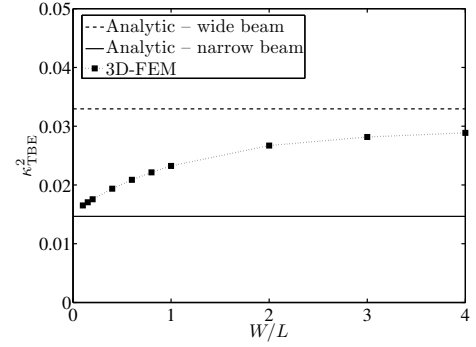


Fig. 11. Electromechanical coupling factor of the TBE device with respect to the beam width for  $t_p/t_b = 0.1$ .

material are calculated and listed in Table I. The effective piezoelectric parameters in the wide beam case are shown in Table II.

### B. Electromechanical coupling of TBE transducer

Figure 10 compares the electromechanical coupling factor of the TBE transducer calculated by 2D FEM and (24). Analytical and FEM results are nearly equal. The wide beam case has larger electromechanical coupling factor than the narrow case. This is because the  $y$ -deformation restriction from narrow to wide beam increase the effective electromechanical coupling factor of the material  $\kappa_{31}^2$  as shown in Table I and Table II.

In Fig.11 we consider a finite beam width using 3D FEM. The numerical electromechanical coupling factor increases monotonically with  $W$  from a value near the analytical narrow-beam result and approaches the analytical wide-beam result.

### C. Two-port model of the symmetric IDE device

We now apply the CMT [19] to calculate the capacitance in our transformations (48) of the symmetric IDE structure Fig.6a. We choose  $a = 3T/4 = 30\mu\text{m}$ . We use the Hilbert transformation [39], [40] to calculate the elliptic integral ratio ( $K(k)/K(k')$  in standard mathematical notation).

Influence on the capacitances of other layers i.e., glass and air, can be taken into account using the partial capacitance

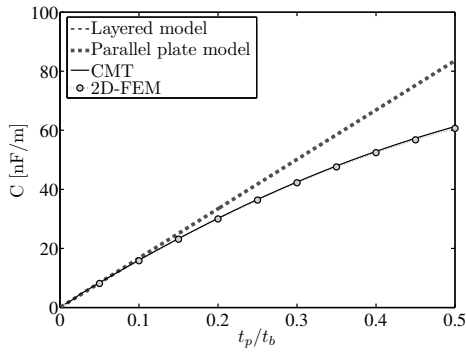


Fig. 12. Capacitance per unit width of the symmetric IDE beam. All  $d_{ij}$  coefficients are artificially set to zero.

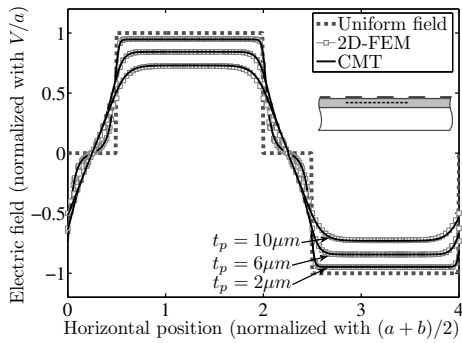


Fig. 13. The normalized electric field along the inset's dotted line at the middle of the piezoelectric layer. All  $d_{ij}$  coefficients are artificially set to zero.

method as mentioned in [19]. With our numerical values, including the high relative permittivity of the piezoelectric material, the total parasitic capacitance from the air and glass layer is less than 10% of the piezoelectric contribution to capacitance if the piezoelectric layer thickness is more than 2.5% (500nm) of the glass thickness. In typical thin-film applications with piezoelectric layer thickness ranging from 1 to 4  $\mu\text{m}$ , the total parasitic capacitance accounts for only 1.25% to 5% of the capacitance. Hence, these parasitic capacitances are neglected.

Figure 12 presents the capacitance of the symmetric IDE structure calculated with different methods: the layered model (33), the parallel plate model ((33) with  $\alpha_{33} = 0$ ), the CMT model- Section IV-A, and a 2D FEM model for the narrow-beam parameters. Here, all piezoelectric coupling constants  $d_{ij}$  are artificially set to zero in order to first understand the electrostatics. In the CMT model, the piezoelectric layer is treated as isotropic with  $\varepsilon_{\text{eq}} = \sqrt{\varepsilon_{33,\text{eff}}\varepsilon_{11}^T}$  and  $\hat{t}_p = t_p \sqrt{\varepsilon_{33,\text{eff}}/\varepsilon_{11}^T}$ .

In Fig.12, no differences are observed between the layered model and the parallel plate model because of the lack of coupling. These simple models predict a linear relationship between the capacitance and the dielectric thickness because of the assumptions of a uniform field distribution (Fig.3). The CMT and FEM results are almost identical. The two models predict smaller capacitances than the layered model. The differences increase with piezoelectric thickness and deviate from the simple linear relationship due to nonuniform electrostatic

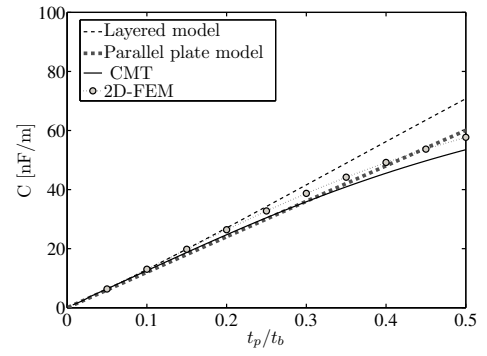


Fig. 14. Capacitance per unit width of the symmetric IDE piezoelectric narrow beam.

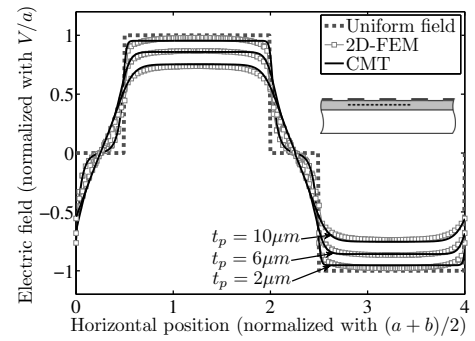


Fig. 15. The normalized electric field along the inset's dotted line at the middle of the piezoelectric layer.

field.

The  $x$ -component of the electric field along the longitudinal direction at the middle of the piezoelectric layer is shown in Fig.13 for zero coupling. The CMT and FEM results are similar. The uniform field model overestimates the electric field strength in the active regions. The overestimation increase with piezoelectric film thickness.

In Fig.14 and Fig.15, we reinstated the correct values of the piezoelectric coupling constants  $d_{ij}$ . In Fig.14, we observe smaller capacitances than in Fig.12. The effect is contained in  $\varepsilon_{33,\text{eff}}$  (34) which also appears in (46). For nonzero coupling it differs from  $\varepsilon_{33}^T$  and depends on the flexural-rigidity ratio.

The capacitance result for the parallel plate model have a manifestly different slope from the layered model whose slope agrees with the other two for small piezoelectric thickness. This is because the flexural rigidity ratio  $\alpha_{33}$  is not taken into account in the parallel plate model.

The  $x$ -component of the electric field is shown in Fig.15. In the active regions, the electric field calculated by the uniform field model is higher than the CMT and the FEM results. The parameters  $\gamma$  and  $\beta$  for the phenomenological quadratic model (PQ model) (55) can be extracted from the CMT or FEM curves in this figure using field values at the center and boundary of the active region as previously described for the CMT in (56) and (57). The results are shown in Fig.16 for different piezoelectric thicknesses. The coefficient  $\gamma$  parametrizing the field at the center of the active regions is always less than one and decreases with the piezoelec-

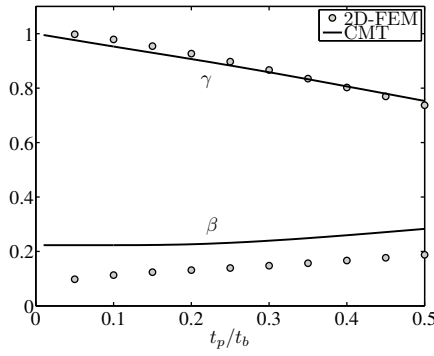


Fig. 16. Fitting parameter of the phenomenological electric field model with 2D-FEM and CMT model.

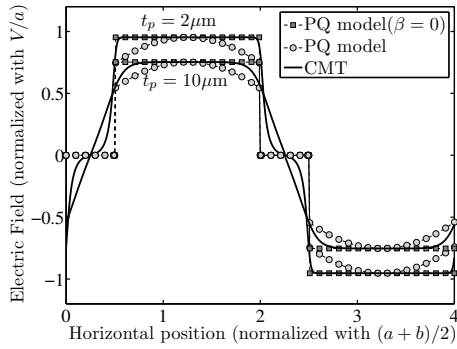


Fig. 17. The phenomenological quadratic model (PQ model) (55) is fitted with the CMT model.

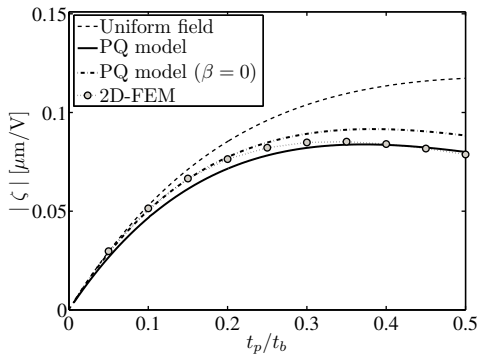


Fig. 18. The coupling constant of the symmetric IDE piezoelectric narrow beam with different electric field model.

tric layer thickness. Hence, the uniform field model always overestimates the electric field. The overestimation increases with the thickness of the piezoelectric layer. The coefficient  $\beta$  parametrizing the flatness increases with the piezoelectric layer thickness. Hence, the quadratic term becomes more important for the thick piezoelectric layer.

The comparison between the PQ model (55) with the CMT is shown in Fig.17. For both cases, especially with the thinner piezoelectric layer, the electric field curve is flat in most of the active region and there is a sharp drop around the edges of the electrode. Hence, the quadratic form does not fit well. We observed that the PQ model (55) without the quadratic term, or  $\beta = 0$ , fits better with the CMT results.

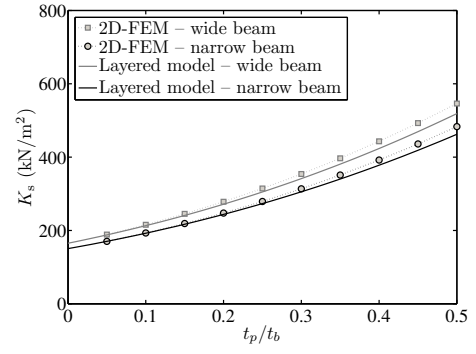


Fig. 19. The stiffness per unit width of the symmetric IDE piezoelectric beam.

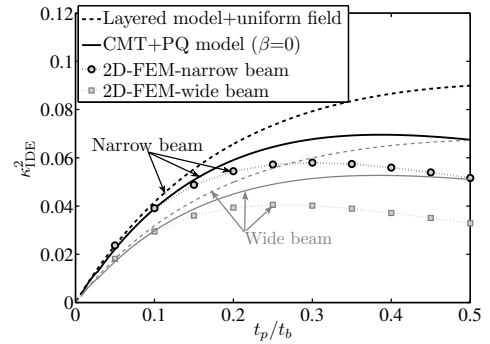


Fig. 20. The electromechanical coupling factor value of the symmetric IDE piezoelectric beam.

Figure 18 shows how the electric field affects the coupling constant  $\zeta$ . The phenomenological model (58) with  $\beta$  equal to or different from zero is closest to the FEM results. In the most interesting thickness range, i.e.,  $t_p \leq 0.2t_b = 4\mu\text{m}$ , (58) with  $\beta = 0$  is closest to the FEM results. Because the uniform field model always overestimates the electric field, it also overestimates the coupling constant  $\zeta$ . However, in the thickness range  $t_p \leq 0.1t_b = 2\mu\text{m}$ , since  $\gamma$  is approximately one in Fig.16, the results of the uniform field and the fitted model (58) with  $\beta = 0$  are both good approximations. For thicker piezoelectric layer i.e.,  $t_p > 0.3t_b$ , the electric fields are less uniform, indicated by the increasing of  $\beta$  in Fig.16, hence, the full PQ model (58) could be a better approximation for the coupling constant  $\zeta$  as shown in Fig.18.

Since all two-port parameters e.g., the free capacitance in Fig.14, the stiffness (37) in Fig.19 and the coupling constant (58) Fig.18 are known, the electromechanical coupling factor can be found. In contrast with the TBE case, the electromechanical coupling factor of the symmetric IDE is larger for a narrow beam than for a wide beam as shown in Fig.20. The reason is the differences in effective electromechanical coupling factor for the material shown in Table I and Table II.

In Fig.20, the electromechanical coupling factor calculated by the layered model with the uniform field assumption is always larger than the FEM and CMT results. The reason is the overestimation of the uniform field model in Fig.15. For the thick piezoelectric layer, even with an undesired compensation made by the capacitance overestimation Fig.14,

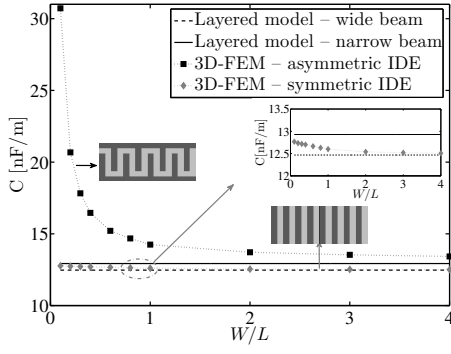


Fig. 21. Capacitance per overlap width  $B$  of the symmetric - asymmetric IDE device at  $g = 5\mu\text{m}$ .

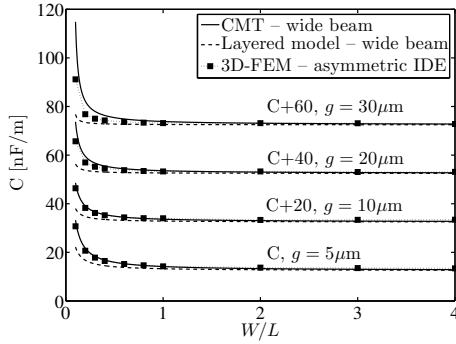


Fig. 22. Capacitance per overlap width  $B$  of the asymmetric IDE device with different end gaps  $g$ .

the electromechanical coupling factor of the layered model is still higher than the FEM and the CMT results. For the thin piezoelectric layer i.e.,  $t_p \leq 0.1t_b = 2\mu\text{m}$ , the overestimate is very small so the results of the two analytic (layered model and CMT with  $\beta = 0$ ) and the FEM models are almost equal.

Note the difference between narrow and wide beam results in Fig.10 and Fig.20. In Fig.10 for the TBE beams, the electromechanical coupling factor is higher for the wide beams while in Fig.20 for the IDE beams, it is higher for the narrow-beam case. This is consistent with the opposite change of effective electromechanical coupling factor in 31-coupling and 33-coupling from narrow-beam case in Table I to wide-beam case in Table II.

#### D. Two-port model of the asymmetric IDE device

The IDE beam studied in this Section has an asymmetric electrode structure due to the interconnect lines shown in Fig.6b. As we discussed in Section IV-C, the CMT is applicable if the electrostatic field is uniformly distributed across the piezoelectric layer thickness. We observed in Section V-C that the field distribution can be assumed uniform if the piezoelectric layer thickness is in the range  $t_p \leq 0.1t_b$ . We choose the beam with dimensions  $t_p = t_b/10 = 2\mu\text{m}$  and keep the gap and the pitch values, i.e.  $a = 3T/4 = 30\mu\text{m}$ .

Adapting the results of Section IV-A, the modified dielectric constant  $\varepsilon_{33,\text{eff}}$  is used instead of  $\varepsilon_{33}^T$ . Hence, the nonzero flexural-rigidity ratio  $\alpha_{33}$  is taken into account. For the CMT model, the partial capacitances  $C_{n1}$  and  $C_{n2}$  in Fig.9 are

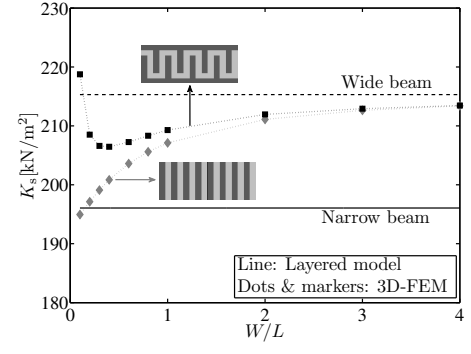


Fig. 23. The IDE beam's short circuit stiffness  $K$  per unit width.

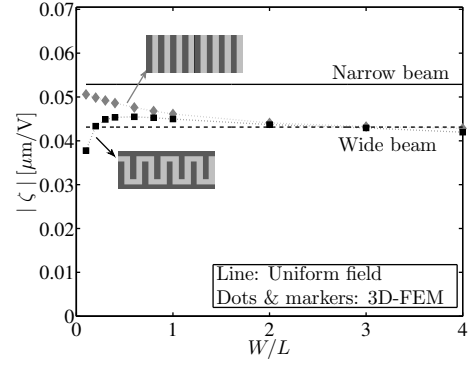


Fig. 24. The coupling constant of the IDE beam.

calculated with the equivalent permittivity  $\varepsilon_{n1}$  and  $\varepsilon_{n2}$  and effective dimensions  $\hat{a}$  and  $\hat{g}$  as given in the Appendix.

Figure 21 compares the capacitance per overlap width  $B$  of the layered model to the FEM result for IDE devices with and without interconnect lines. For the symmetric IDE beam, the two layered-model capacitances with narrow and wide beam parameters set respectively the upper and lower limits of the FEM results. The capacitance of the FEM model decreases asymptotically towards the wide-beam limit as the beam width is increased. This is because the effective dielectric constant decreases from  $\varepsilon_{33}^T$  to  $\varepsilon_{33,\text{eff}}^T$  as shown in Table I and Table II.

For the asymmetric IDE beam, additional capacitance around the end gap of the IDE fingers contributes. This explains why the capacitance per overlap width is higher with the asymmetric than with the symmetric IDE.

In order to improve the layered model, we have added the capacitance between the end of each electrode finger and the interconnect line using the same approach as for the inter-electrode capacitance. The result is compared to CMT and FEM in Fig.22. The layered model with narrow-beam parameters is not shown because it is visually indistinguishable from the wide-beam result. The total capacitance per overlap width is still smaller than the FEM results especially if  $W/L < 1$ . This means there are additional contributions caused by the fringing effects at the corners of the IDE fingers. By applying the CMT technique, these fringing capacitances are taken into account. The CMT model is in a better agreement with the FEM results. Therefore, the CMT model is more accurate than the layered model.

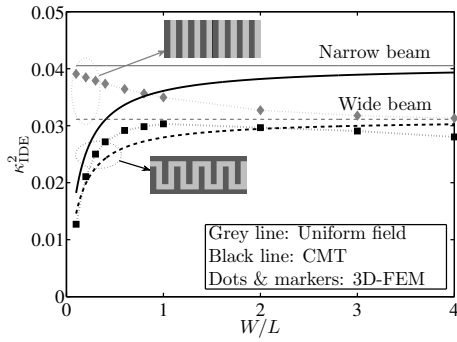


Fig. 25. Electromechanical coupling factor of the IDE beam with  $g = 5\mu\text{m}$ .

Using the capacitance  $C$  of the layered model with end-gaps in Fig.22 or without end-gaps in Fig.21, the stiffness  $K_s$  (37) in Fig.23, and the coupling constant  $\zeta$  (31) in Fig.24, we can find the electromechanical coupling factor of the symmetric and asymmetric IDE beams. The results are shown in Fig.25. The asymmetric IDE beam has smaller electromechanical coupling factor than the symmetric one. The reason is the parasitic capacitance around the end gaps of the asymmetric IDE configuration. For the symmetric IDE beam, the FEM results are bracketed between the narrow- and wide-beam results. The situation is more complex for the asymmetric IDE beam. For this configuration, if  $W$  is small, i.e.  $W < L$ , the FEM results increase significantly with the width  $W$ . The dramatic change comes from the change in the capacitance. The CMT model (darker solid and dashed line) is capable of capturing this feature. We note that the CMT result with wide-beam parameters is significantly closer to the FEM result than the CMT with narrow-beam parameters, also for rather small  $W/L$ . This observation suggests that the CMT-model with wide-beam parameters is preferable.

#### E. Comparison between TBE and IDE transducers

The ratio between the electromechanical coupling factor of the IDE beam in Fig.25 to that of the TBE beam in Fig.11 is shown in Fig.26. We first consider the symmetric configuration. In this case the layered model without end-gap effects, brackets the ratio from the FEM calculation. The wide-beam parameters give a lower bound and the narrow-beam parameters give an upper bound. This is similar to what we observed for the electromechanical coupling factor of the IDE beam in Fig.25 and the TBE beam in Fig.11.

In our case, the lower limit of the ratio is approximately one as shown in Fig.26. Hence, the IDE beam always has higher electromechanical coupling factor than the TBE counterpart. The conclusion is confirmed by FEM results. The symmetric IDE beam always has larger electromechanical coupling factor than the TBE beam and is therefore preferable if coupling is the decisive parameter. However, if one instead considers tip-deflection, one finds instead that the TBE is preferable [24], [41].

The same conclusion is arrived at for the asymmetric IDE beam with  $W/L > 0.15$ . The maximum ratio of electrome-

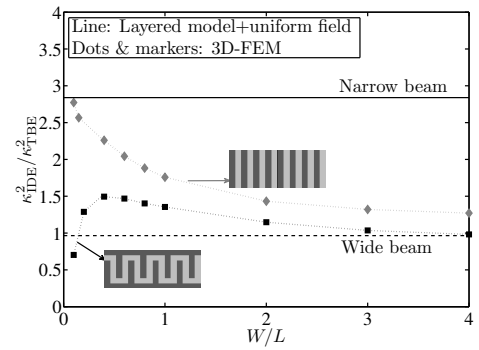


Fig. 26. Electromechanical coupling factor ratio of the IDE device to the TBE ones.

chanical coupling factors is found for  $W/L \approx 0.4$ , i.e.  $L = 1000\mu\text{m}$  and  $W = 400\mu\text{m}$ , which gives a ratio of 1.5.

## VI. CONCLUSION

The linear two-port models of piezoelectric layered beams with transversal and longitudinal coupling were investigated. Because theory for the TBE beam is well-established, this paper made further effort in completing the two-port model for the IDE beam. While the short-circuit stiffness of the IDE beam can be approximated by layered-beam theory, the capacitance and the transducer coupling constant required new theory.

First, the conformal mapping technique was adapted to apply to anisotropic dielectric materials. We found that the capacitance of the piezoelectric structure, like a structure with merely an anisotropic dielectric, can be treated as an isotropic dielectric structure with an equivalent permittivity and equivalent dimensions without neglecting the piezoelectric coupling. The effective, relative permittivity of the piezoelectric material depends on the electromechanical coupling factor of the material and a ratio of flexural rigidities.

Based on the transformation of the original problem to the effective isotropic problem, formulas for the capacitance and the electric field were derived. The electric field formula was simplified to a quadratic form. Then, the transducer coupling constant was found directly.

By this, we achieved analytical results for all parameters of the linear two-port model of an IDE beam despite the complexity brought on by the anisotropic material parameters and complicated electrode structure. All analytical results were compared to finite element calculations.

The two-port model was used to compare the device electromechanical coupling factors of the piezoelectric beams with IDE and TBE configurations. Judging by this performance figure, we found that the IDE is favourable except for very narrow beams. This is the different conclusion from what one obtains if the device is instead judged only by its free tip-deflection. In our particular example, we found that the IDE beam can be designed with up to 1.5 times higher electromechanical coupling factor than the TBE beam.

## APPENDIX ANALYTIC MODEL SUMMARY

Table III contains necessary formulas to calculate the two-port parameters for the piezoelectric narrow beam. For the wide beam, the effective values (3), (4) and (7) should be used instead. Table IV classifies and summaries all physical models for the IDE beam.

### ACKNOWLEDGMENT

This work was supported by the Research Council of Norway through Grant no. 235210. Some of our FEM calculations were performed on the Abel Cluster owned by the University of Oslo and the Norwegian Metacenter for High Performance Computing (NOTUR) and were supported by Grant no. NN9344K.

### REFERENCES

- [1] S. Roundy and P. K. Wright, "A piezoelectric vibration based generator for wireless electronics," *Smart Materials and Structures*, vol. 13, pp. 1131–1142, 2004.
- [2] D. L. DeVoe and A. P. Pisano, "A fully surface-micromachined piezoelectric accelerometer," in *Solid State Sensors and Actuators, 1997. TRANSDUCERS '97 Chicago., 1997 International Conference on*, vol. 2, Jun 1997, pp. 1205–1208 vol.2.
- [3] M. Klee, M. D. Esch, W. Keur, B. Kumar, L. V. Leuken-peters, J. Liu, R. Mauczok, K. Neumann, K. Reimann, C. Renders, A. L. Roest, M. P. J. Tiggelman, M. D. Wild, O. Wunnicke, and J. Zhao, "Ferroelectric thin-film capacitors and piezoelectric switches for mobile communication applications," *IEEE Transactions on Ultrasonics, Ferroelectrics, and Frequency Control*, vol. 56, no. 8, pp. 1505–1512, August 2009.
- [4] K. H. Koh, T. Kobayashi, F.-L. Hsiao, and C. Lee, "Characterization of piezoelectric PZT beam actuators for driving 2D scanning micromirrors," *Sensors and Actuators A: Physical*, vol. 162, no. 2, pp. 336 – 347, 2010, eurosensors XXIII, 2009.
- [5] I. G. Mina, H. Kim, I. Kim, S. K. Park, K. Choi, T. N. Jackson, R. L. Tutwiler, and S. Trolier-McKinstry, "High frequency piezoelectric MEMS ultrasound transducers," *IEEE Transactions on Ultrasonics, Ferroelectrics, and Frequency Control*, vol. 54, no. 12, pp. 2422–2430, December 2007.
- [6] J. G. Smits and W. Choi, "The constituent equations of piezoelectric heterogeneous bimorphs," *IEEE Transactions on Ultrasonics, Ferroelectrics, and Frequency Control*, vol. 38, no. 3, pp. 256–270, May 1991.
- [7] J. G. Smits, S. I. Dalke, and T. K. Cooney, "The constituent equations of piezoelectric bimorphs," *Sensors and Actuators A: Physical*, vol. 28, no. 1, pp. 41 – 61, 1991.
- [8] Q.-M. Wang, X.-H. Du, B. Xu, and L. E. Cross, "Electromechanical coupling and output efficiency of piezoelectric bending actuators," *IEEE Transactions on Ultrasonics, Ferroelectrics, and Frequency Control*, vol. 46, no. 3, pp. 638–646, May 1999.
- [9] P. Murali, R. G. Polcawich, and S. Trolier-McKinstry, "Piezoelectric thin films for sensors, actuators, and energy harvesting," *MRS Bulletin*, vol. 34, pp. 658–664, 9 2009.
- [10] J. B. Jaffe, W. R. Cook and H. Jaffe, *Piezoelectric Ceramics*. London: Academic Press, 1971.
- [11] K. Uchino, *Piezoelectric Actuators and Ultrasonic Motors*. Boston, MA: Kluwer, 1996.
- [12] Y. Jeon, R. Sood, J. h. Jeong, and S.-G. Kim, "MEMS power generator with transverse mode thin film PZT," *Sensors and Actuators A: Physical*, 2005.
- [13] S. J. Gross, S. Tadigadapa, T. N. Jackson, S. Trolier-McKinstry, and Q. Q. Zhang, "Lead-zirconate-titanate-based piezoelectric micromachined switch," *Applied Physics Letters*, vol. 83, no. 1, 2003.
- [14] Z. Shen, C. Y. Tan, K. Yao, L. Zhang, and Y. F. Chen, "A miniaturized wireless accelerometer with micromachined piezoelectric sensing element," *Sensors and Actuators A: Physical*, vol. 241, pp. 113 – 119, 2016.
- [15] C. H. Nguyen, M. A. Farghaly, M. N. Akram, U. Hanke, and E. Halvorsen, "Electrode configurations for layered-plate piezoelectric micro-actuators," *Microelectronic Engineering*, vol. 174, pp. 59 – 63, 2017.
- [16] C. Mo, S. Kim, and W. W. Clark, "Theoretical analysis of energy harvesting performance for unimorph piezoelectric benders with interdigitated electrodes," *Smart Materials and Structures*, vol. 18, no. 5, p. 055017, 2009.
- [17] J. C. Park, J. Y. Park, and Y. P. Lee, "Modeling and characterization of piezoelectric  $d_{33}$  -mode MEMS energy harvester," *Journal of Microelectromechanical Systems*, vol. 19, no. 5, pp. 1215–1222, Oct 2010.
- [18] S.-B. Kim, J.-H. Park, S.-H. Kim, H. Ahn, H. C. Wickle, and D.-J. Kim, "Modeling and evaluation of  $d_{33}$  mode piezoelectric energy harvesters," *Journal of Micromechanics and Microengineering*, vol. 22, no. 10, p. 105013, 2012.
- [19] R. Igreja and C. Dias, "Analytical evaluation of the interdigital electrodes capacitance for a multi-layered structure," *Sensors and Actuators A: Physical*, vol. 112, no. 23, pp. 291 – 301, 2004.
- [20] M. Kim, J. Dugundji, and B. L. Wardle, "Effect of electrode configurations on piezoelectric vibration energy harvesting performance," *Smart Materials and Structures*, vol. 24, no. 4, p. 045026, 2015.
- [21] J. Wei, "Distributed capacitance of planar electrodes in optic and acoustic surface wave devices," *IEEE Journal of Quantum Electronics*, vol. 13, no. 4, pp. 152–158, April 1977.
- [22] T. Ikeda, *Fundamentals of piezoelectricity*. Oxford University Press, 1990.
- [23] M. Weinberg, "Working equations for piezoelectric actuators and sensors," *Microelectromechanical Systems, Journal of*, vol. 8, no. 4, pp. 529–533, Dec 1999.
- [24] C. H. Nguyen, U. Hanke, and E. Halvorsen, "Actuation of piezoelectric layered beams with  $d_{31}$  and  $d_{33}$  coupling," *IEEE Transactions on Ultrasonics, Ferroelectrics, and Frequency Control*, vol. 65, no. 5, pp. 815–827, May 2018.
- [25] S. K. Kaldor and I. C. Noyan, "Differentiating between elastically bent rectangular beams and plates," *Applied Physics Letters*, vol. 80, no. 13, pp. 2284–2286, 2002.
- [26] S. R. Swanson, "Anticlastic effects and the transition from narrow to wide behavior in orthotropic beams," *Composite Structures*, vol. 53, no. 4, pp. 449 – 455, 2001.
- [27] E. Tadmor and G. Kosa, "Electromechanical coupling correction for piezoelectric layered beams," *Microelectromechanical Systems, Journal of*, vol. 12, no. 6, pp. 899–906, Dec 2003.
- [28] "IEEE standard on piezoelectricity," *ANSI/IEEE Std 176-1987*, 1988.
- [29] J. F. Nye, *Physical Properties of Crystals-Their representation by Tensors and Matrices*. Oxford University Press, 1985.
- [30] R. Nigon, T. M. Raeder, and P. Murali, "Characterization methodology for lead zirconate titanate thin films with interdigitated electrode structures," *Journal of Applied Physics*, vol. 121, no. 20, p. 204101, 2017.
- [31] R. R. Knight, C. Mo, and W. W. Clark, "MEMS interdigitated electrode pattern optimization for a unimorph piezoelectric beam," *Journal of Electroceramics*, vol. 26, no. 1, pp. 14–22, 2011.
- [32] E. Weber, *Electromagnetic Theory: Static fields and their mapping*. Dover Publications, Inc., New York, 1965.
- [33] S. S. Gevorgian, T. Martinsson, P. L. J. Linner, and E. L. Kollberg, "CAD models for multilayered substrate interdigital capacitors," *IEEE Transactions on Microwave Theory and Techniques*, vol. 44, no. 6, pp. 896–904, Jun 1996.
- [34] O. Ramer, "Integrated optic electrooptic modulator electrode analysis," *IEEE Journal of Quantum Electronics*, vol. 18, no. 3, pp. 386–392, Mar 1982.
- [35] N. Chidambaram, A. Mazzalai, D. Balma, and P. Murali, "Comparison of lead zirconate titanate thin films for microelectromechanical energy harvester with interdigitated and parallel plate electrodes," *IEEE transactions on ultrasonics, ferroelectrics, and frequency control*, vol. 60, no. 8, pp. 1564–1571, 2013.
- [36] T. M. Raeder, "Self-Poling and Ageing in PZT Thin Films With Interdigitated Electrodes," Master's thesis, NTNU, Norway, 2015.
- [37] N. Ledermann, P. Murali, J. Baborowski, S. Gentil, K. Mukati, M. Cantoni, A. Seifert, and N. Setter, "1 0 0-textured, piezoelectric  $\text{Pb}(\text{Zr}_x\text{Ti}_{1-x})\text{O}_3$  thin films for MEMS: integration, deposition and properties," *Sensors and Actuators A: Physical*, vol. 105, no. 2, pp. 162 – 170, 2003.
- [38] M.-A. Dubois, P. Murali, D. V. Taylor, and S. Hiboux, "Which PZT thin films for piezoelectric microactuator applications?" *Integrated Ferroelectrics*, vol. 22, no. 1-4, pp. 535–543, 1998.
- [39] W. Hilberg, "From approximations to exact relations for characteristic impedances," *IEEE Transactions on Microwave Theory and Techniques*, vol. 17, no. 5, pp. 259–265, May 1969.
- [40] C. H. Nguyen, R. Nigon, T. M. Raeder, U. Hanke, E. Halvorsen, and P. Murali, "Probing-models for interdigitated electrode systems with

TABLE III  
ANALYTIC MODEL SUMMARY

	TBE	Symmetric IDE	Asymmetric IDE
	Short-circuit stiffness $\hat{K}_s$		
Layered model	$\frac{3W\hat{K}}{L^3}$	$\frac{3W\hat{K}_2}{L^3}$	$\frac{3W\hat{K}_2}{L^3}$
Definition	$\hat{K} = \sum_m Y_m \left[ \frac{I_m}{1-\kappa_m^2} + t_m \bar{z}_m^2 \right],$ $Y_p = \frac{1}{s_{11}^E}, \quad \kappa_p^2 = \kappa_{31}^2 = \frac{d_{31}^2}{s_{11}^E \epsilon_{33}^T},$ $\bar{z}_m = \frac{z_{m+1} + z_m}{2}, \quad \sum_m \bar{z}_m Y_m t_m = 0,$ $I_m = t_m^3/12 \text{ and } t_m = z_{m+1} - z_m.$	$\hat{K}_2 = \sum_m Y_m [I_m + t_m \bar{z}_m^2],$ $Y_p = \frac{1}{s_{33}^E},$ $\bar{z}_m = \frac{z_{m+1} + z_m}{2}, \quad \sum_m \bar{z}_m Y_m t_m = 0,$ $I_m = t_m^3/12 \text{ and } t_m = z_{m+1} - z_m.$	$\hat{K}_2 = \sum_m Y_m (I_m + t_m \bar{z}_m^2),$ $Y_p = \frac{1}{s_{33}^E},$ $\bar{z}_m = \frac{z_{m+1} + z_m}{2}, \quad \sum_m \bar{z}_m Y_m t_m = 0,$ $I_m = t_m^3/12 \text{ and } t_m = z_{m+1} - z_m.$
	Free capacitance $C$		
Parallel plate model	$N \epsilon_{33}^T (1 - \kappa_{33}^2) \frac{W t_p}{a}$		
Layered model	$\epsilon_{33}^T [1 + (\alpha_{31} - 1) \kappa_{31}^2] \frac{WL}{t_p}$	$N \epsilon_{33,\text{eff}} \frac{W t_p}{a}$	$N \left( \epsilon_{33,\text{eff}} \frac{B t_p}{a} + \epsilon_{31,\text{eff}} \frac{b t_p}{g} \right)$
CMT		$\frac{NW}{2} \epsilon_{eq} \frac{K(k_I)}{K(k_I')}$	$\frac{2N t_p}{\pi} (\epsilon_{n1} \ln \frac{1}{\theta_{n1,3'}} + \epsilon_{n2} \ln \theta_{n2,1'})$
Definition	$\alpha_{31} = \frac{t_p \bar{z}_p^2}{s_{11}^E \hat{K}}.$	$\epsilon_{33,\text{eff}} = \epsilon_{33}^T [1 + (\alpha_{33} - 1) \kappa_{33}^2],$ $\alpha_{33} = \frac{t_p \bar{z}_p^2}{s_{33}^E \hat{K}_2}, \quad \kappa_{33}^2 = \frac{d_{33}^2}{s_{33}^E \epsilon_{33}^T},$	$\epsilon_{33,\text{eff}} = \epsilon_{33}^T [1 + (\alpha_{33} - 1) \kappa_{33}^2],$ $\alpha_{33} = \frac{t_p \bar{z}_p^2}{s_{33}^E \hat{K}_2}, \quad \kappa_{33}^2 = \frac{d_{33}^2}{s_{33}^E \epsilon_{33}^T},$ $\epsilon_{31,\text{eff}} = \epsilon_{33}^T [1 + (\alpha_{31,n2} - 1) \kappa_{31}^2],$ $\alpha_{31,n2} = \frac{t_p \bar{z}_p^2}{s_{11}^E \hat{K}_2}, \quad \kappa_{31}^2 = \frac{d_{31}^2}{s_{11}^E \epsilon_{33}^T},$
		$\epsilon_{eq} = \sqrt{\epsilon_{33,\text{eff}} \epsilon_{11}^T},$ $k_I = \sqrt{1 - k_1'^2} = \frac{q(b/2)\sqrt{1-k^2}}{\sqrt{1-k^2}q(X_2)^2},$ $q(X) = \text{sn} \left( \frac{2K(k)X}{a+b}, k \right),$ $k = \sqrt{1 - k_1'^2}, \quad \frac{K(k')}{K(k)} = \frac{2\hat{t}_p}{a+b},$ $\text{and } \hat{t}_p = t_p \sqrt{\epsilon_{33,\text{eff}}/\epsilon_{11}^T}.$	$\epsilon_{n1} = \sqrt{\epsilon_{33,\text{eff}} \epsilon_{11}^T}, \quad \epsilon_{n2} = \sqrt{\epsilon_{31,\text{eff}} \epsilon_{11}^T},$ $\theta_{n1,3'} \text{ is the solution of the following equation}$ $\frac{B}{2} = \frac{g}{\pi} \left[ 2 \sinh^{-1} \sqrt{\frac{\theta-1}{p_{n1}+1}} - \frac{2 \tan^{-1} \sqrt{\frac{p_{n1}(\theta-1)}{\theta+p_{n1}}}}{\sqrt{p_{n1}}} \right]$ $\text{with } p_{n1} = \frac{g^2}{\hat{a}^2} \quad \text{and} \quad \hat{a} = a \sqrt{\epsilon_{11}^T/\epsilon_{33,\text{eff}}}.$ $\theta_{n2,1'} \text{ is the solution of the following equation}$ $\frac{b}{2} = \frac{\hat{g}}{\pi} \left[ 2 \sinh^{-1} \sqrt{\frac{\theta-1}{p_{n2}+1}} - \frac{2 \tan^{-1} \sqrt{\frac{p_{n2}(\theta-1)}{\theta+p_{n2}}}}{\sqrt{p_{n2}}} \right]$ $\text{with } p_{n2} = \frac{\hat{g}^2}{a^2} \quad \text{and} \quad \hat{g} = g \sqrt{\epsilon_{11}^T/\epsilon_{31,\text{eff}}}.$
	Coupling constant $\zeta$		
Uniform field	$\frac{\bar{z}_p d_{31}}{s_{11}^E \hat{K}} \frac{L^2}{2}$	$\frac{\bar{z}_p d_{33} t_p}{s_{33}^E \hat{K}_2} \frac{N^2 a}{2} \left( 1 + \left( 1 + \frac{1}{N} \right) \frac{b}{a} + \frac{2}{N} \right)$	$\frac{\bar{z}_p d_{33} t_p}{s_{33}^E \hat{K}_2} \frac{N^2 a}{2} \left( 1 + \left( 1 + \frac{1}{N} \right) \frac{b}{a} + \frac{2}{N} \right)$
PQ model ( $\beta = 0$ )		$\gamma \frac{\bar{z}_p d_{33} t_p}{s_{33}^E \hat{K}_2} \frac{N^2 a}{2} \left( 1 + \left( 1 + \frac{1}{N} \right) \frac{b}{a} + \frac{2}{N} \right)$	
Definition		$\gamma = \text{Re} \left[ \mathbf{E} \left( \frac{a+b}{2} + j \frac{\hat{t}_p}{2} \right) \right] \times \frac{a}{V},$ $\mathbf{E}(X) = j \frac{V}{a+b} \frac{K(k)}{K(k_1')} \frac{\sqrt{1-k^2}q(b/2)^2}{\sqrt{q(b/2)^2 - q(X)^2}}$	

TABLE IV  
MODEL SUMMARY FOR THE IDE BEAM

Physical quantities	Notation	Equation
Material properties		
Young modulus	$Y$	(5)
Piezoelectric coupling constant	$d$	(6)
Dielectric constant	$\varepsilon$	(7)
Mechanical quantities		
Flexural rigidity	$\tilde{K}, \tilde{K}_2$	(16), (26)
Short-circuit stiffness	$K_s$	(30), (37)
Second derivative of deflection	$\partial^2 w / \partial x^2$	(25), (43)
Electrical quantities		
Free capacitance	$C$	(33), (59), [19], [40]
Electric field	$\mathbf{E}, E_x$	(50), (54), [40]
Electromechanical quantities		
Coupling constant	$\zeta$	(31), (58)
Electromechanical coupling factor	$\kappa$	(2), (38)

ferroelectric thin films,” *Journal of Physics D: Applied Physics*, vol. 51, no. 17, p. 175303, 2018.

- [41] N. Chidambaram, D. Balma, R. Nigon, A. Mazzalai, R. Matloub, C. S. Sandu, and P. Murralt, “Converse mode piezoelectric coefficient for lead zirconate titanate thin film with interdigitated electrode,” *Journal of Micromechanics and Microengineering*, vol. 25, no. 4, p. 045016, 2015.



**Cuong H. Nguyen** received the M.Sc. degree in micro and nano systems technology from the Buskerud and Vestfold University College, Norway, in 2014, and the Ph.D. degree in applied micro- and nano-systems from the University of South-Eastern Norway, Horten, Norway, in 2018.

His current research interest is in theory, design, modeling, and characterization of microelectromechanical devices.



**Ulrik Hanke** Ulrik Hanke (SM06) received the Siv.Ing. degree and the Dr.Ing. degree in physics from the Norwegian University of Science and Technology (NTNU), Trondheim, Norway, in 1989 and 1994, respectively. After two years as a Post. Doc. he worked for a decade as a research scientist at department of communication technology, SINTEF. Since 2006, he has been with University of South-Eastern Norway, Horten, where he is a Professor of Micro- and Nanosystem technology. His current main research interest is in theory, design, and

modeling of piezoelectric and RF acoustic micro devices.



**Einar Halvorsen** Einar Halvorsen (M03) received the Siv.Ing. degree in physical electronics from the Norwegian Institute of Technology (NTH), Trondheim, Norway, in 1991, and the Dr.Ing. degree in physics from the Norwegian University of Science and Technology (NTNU), Trondheim, Norway, in 1996. He has worked both in academia and the microelectronics industry. He is now with the Department of Microsystems, University of South-Eastern Norway, Horten, Norway, where he is a professor.

His current main research interest is in theory, design and modeling of microelectromechanical devices, in particular actuators and energy harvesting devices.